JAAS

ROYAL SOCIETY OF CHEMISTRY

COMMUNICATION

View Article Online
View Journal

Cite this: DOI: 10.1039/d6ja00085a

Received 8th March 2026
Accepted 20th April 2026

DOI: 10.1039/d6ja00085a

rsc.li/jaas

In situ Rb/Sr dating of potassium salt minerals (sylvite and carnallite) by 157 nm LA-ICP-MS/MS

Martin Kutzschbach, *[ab] Tobias Erhardt, [ab] Michael Mertineit,[c] Linda Marko,[ab] Michael Schramm,[c] Lisa Richter,[c] Wilhelm Nikonow[c] and Wolfgang Müller *[ab]

Evaporite deposits are of increasing societal importance as potential repositories for high-level radioactive waste and host lithologies for the subsurface storage of natural gas and hydrogen. To conduct robust long-term risk assessments (particularly with respect to the timing of deposition and deformation), the geological history of such deposits must be reconstructed accurately. However, direct geochronometric methods applicable to evaporites remain very limited and ages may be obtained only indirectly *via* dating of detrital minerals. We report the first application of reaction-cell laser ablation-inductively coupled plasma-tandem mass spectrometry (LA-ICP-MS/MS), using a recently developed dual-wavelength laser system (193 nm and 157 nm), to potassium salt minerals (sylvite and carnallite) from the Morsleben site (NE Germany), which is hosted within a salt structure of Permian age. Compared with 193 nm, ablation at 157 nm is more controlled and shows less Rb–Sr elemental fractionation. Despite low (6–40 ng g^{-1}) strontium concentrations, the salt minerals contain almost exclusively radiogenic ^{87}Sr (~99%), which enables the determination of precise (~3%) single-spot Rb–Sr ages that are independent of the initial $^{87}Sr/^{86}Sr$. Kernel density estimates of these single-spot ages reveal four dominant age modes at ~4 Ma, ~14 Ma, ~33 Ma and ~91 Ma. These ages are consistent with the few previously published data from Morsleben and nearby salt mines, and could be linked to regional tectonic events. We demonstrate, for the first time, the potential of *in situ* LA-ICP-MS/MS as a direct (and rapid) geochronological tool for evaporite deposits at a spatial resolution of ≤100 μm.

1. Introduction

Evaporite deposits are of considerable societal and economic importance. Besides mineral resources as such, thick salt sequences are widely regarded as suitable host rocks for high-level radioactive waste disposal[1,2] and for underground storage of natural gas and hydrogen[3–5] due to their low permeability, high thermal conductivity and self-healing behavior.[6–8] In addition, potassium-bearing evaporites constitute a critical raw material for fertilizer production.[9] These applications require a detailed understanding of the depositional, diagenetic and deformation history of salt deposits, including robust constraints on the timing of salt deposition and subsequent deformation or fluid–rock interaction.

Radiogenic isotope systems provide powerful tools to constrain the timing of geological processes.[10] They allow the determination of crystallization ages of mineral phases, which can also be reset or partially re-equilibrated during recrystallization and dissolution–reprecipitation processes. Such processes commonly accompany major tectonic events or (hydro)thermal fluid circulation and, therefore, provide a record of deformation, sealing and fluid-flow histories that may overprint evaporite deposits. Isotopic ages, thus, complement structural geological analyses and regional geological reconstructions.

Apart from pioneering studies, relatively few attempts have been made to directly date salt minerals using isotopic methods. These include K–Ar and $^{40}Ar/^{39}Ar$ dating of potassium- and magnesium-bearing sulfates such as polyhalite, leonite, langbeinite, kieserite, and kainite.[11–21] K–Ca dating has been applied to sylvite and carnallite,[22–25] while Sm–Nd dating has been used for intrasalinary magnesite.[26] Rb–Sr dating has also been applied to sylvite, carnallite, and langbeinite.[14,25,27–31]

Importantly, all these examples were limited in spatial resolution. Applications of Sm–Nd, K–Ca, and Rb–Sr geochronometers to salts have required dissolution of substantial amounts of sample material (*e.g.*, gram–kilogram-scale samples for the ID-TIMS of carnallite).[28,30] However, K–Ar and $^{40}Ar/^{39}Ar$ case studies have involved laser heating of comparatively large quantities of material. For example, aliquots of ~50 mg were used for the K–Ar analyses done by Wójtowicz *et al.* in 2003, and several grains of 200–250 μm size were required for the $^{40}Ar/^{39}Ar$ analyses undertaken by Leitner *et al.* in 2022.[18,21] Such bulk or

[a]*Institute of Geosciences, Goethe University Frankfurt, Frankfurt am Main, Germany. E-mail: kutzschbach@em.uni-frankfurt.de; w.muller@em.uni-frankfurt.de*

[b]*Frankfurt Isotope and Element Research Center (FIERCE), Goethe University Frankfurt, Frankfurt am Main, Germany*

[c]*Bundesanstalt für Geowissenschaften & Rohstoffe (BGR), Hannover, Germany*

semi-bulk approaches risk co-analyzing fluid inclusions or mineral impurities, potentially biasing age results. Moreover, small-scale domains affected by recrystallization or dissolution–reprecipitation during fluid interaction are likely to remain undetected.

Laser-based *in situ* dating methods offer substantially higher spatial resolution, typically consuming only a few hundred nanograms of sample material and, hence, offering direct targeting of specific microstructural domains. However, despite their widespread application to silicates (mica, feldspar, amphiboles, zircon), oxides (rutile, magnetite), and phosphates (apatite, monazite), such methods have not been applied to salt minerals. The only notable exception is *in situ* U–Pb dating of sulfates such as gypsum and anhydrite,[32,33] which are common constituents of evaporite sequences. Other *in situ* geochronological applications in salt-bearing successions have focused on accessory minerals embedded within the salt formation, such as volcanic apatite or detrital zircon and rutile, to indirectly constrain depositional ages.[34,35]

Potassium-bearing salt minerals, particularly sylvite (KCl) and carnallite ($KMgCl_3 \cdot 6H_2O$), represent promising targets for *in situ* Rb–Sr geochronology using laser ablation-inductively coupled plasma-tandem mass spectrometry (LA-ICP-MS/MS). These minerals are widespread primary (for sylvite under the condition of $MgSO_4$-depleted seawater) and secondary constituents of evaporite deposits. Also, due to the similar ionic radii of Rb^+ and K^+,[36] they are expected to contain increased Rb concentrations, yet little common-Sr, resulting in increased Rb/Sr-ratios and, thus, sufficient ingrowth of radiogenic ^{87}Sr. Furthermore, compared with the K–Ar system, the Rb–Sr system is expected to be more retentive during secondary (hydro) thermal events.[37,38] This hypothesis is supported by the lower closure temperatures reported for K–Ar in muscovite (approximately 350–450 °C) relative to Rb–Sr in muscovite (approximately 500–650 °C).[39–44] No systematic study has examined the relative closure temperatures of the K–Ar and Rb–Sr systems in K-salt minerals. Nevertheless, early investigations into the retentivity of Ar in sylvite indicated that Ar diffusion increases drastically at temperatures exceeding 40 °C.[45,46] Moreover $^{40}Ar/^{39}Ar$ geochronology requires neutron irradiation, which involves access to nuclear facilities, handling of activated materials and, hence, imposes significant logistical constraints. As a result, the time from sample preparation to analyses can extend over several months. Even after irradiation, individual analyses typically require approximately 1–2 h, which is considerably longer than *in situ* Rb–Sr measurements by LA-ICP-MS/MS. Solution-based ID-TIMS Rb–Sr dating has been applied to salt minerals and there have been successful attempts to overcome limitations in spatial resolution through microdrilling and laser-cutting sampling techniques, which have reduced ID-TIMS sample sizes to a few tens of micrograms.[47,48] However, these μ-ID-TIMS studies targeted Sr-rich minerals such as mica, which contain several tens of $\mu g\ g^{-1}$ Sr and exhibit comparatively moderate $^{87}Rb/^{86}Sr$ ratios (often <100). This is contrasted by K-salt minerals, which are typically characterized by extreme $^{87}Rb/^{86}Sr$ ratios (up to several million) and low Sr concentrations (down to <10 ng g^{-1}).[29] This poses two analytical challenges. First, the extremely high Rb/Sr ratios complicate the separation of Rb and Sr in conventional wet-chemical approaches and residual ^{87}Rb may cause isobaric interference on ^{87}Sr.[49,50] In contrast, the separation of Rb and Sr using a collision reaction cell (CRC) in LA-ICP-MS/MS is considered quantitative. Within the CRC, reactive gases (O_2, SF_6, N_2O, CH_3F) form Sr-molecule ions such as SrF^+ or SrO^+ that can be measured free of ^{87}Rb-interference.[51–55] The efficiency of the CRC-based purification process has been demonstrated by Zack & Hogmalm.[51] When using O_2 as a reactive gas, they observed no detectable signal at mass 101 ($^{85}Rb^{16}O$) during ablation of pure RbCl, despite a signal of 10^9 cps on mass 85 (^{85}Rb). Second, the very low Sr concentrations in K salts necessitate stringent blank control and, ultimately, increase the minimum amount of sample required for a single analysis. In previous studies, the total mass of Sr analyzed was typically <10 ng, while blank levels were maintained at <10 pg, corresponding to ~1‰ blank contributions.[47,48] Given that Sr concentrations in K salts are roughly three-orders of magnitude lower than in mica (ng g^{-1} *vs.* μg g^{-1}), achieving 1‰ blank levels would require a proportional increase in sample size on the order of tens of milligrams. Consequently, the spatial resolution offered by LA-ICP-MS/MS is effectively unattainable using ID-TIMS. Third, ID-TIMS typically requires several days per sample, including dissolution, spike equilibration, and chromatographic purification, with measurement times lasting several hours. Consequently, analytical throughput is limited to only a few samples per month per instrument. In contrast, LA-ICP-MS/MS enables *in situ* measurements within minutes, representing an improvement in throughput of several orders of magnitude.

In this study, we present the first successful laser-based *in situ* Rb–Sr dating of the K-salt minerals sylvite and carnallite. And thus demonstrate the feasibility of high-spatial-resolution geochronology directly applied to evaporite minerals. This advance was enabled by exploiting the superior ablation behavior of K salts at 157 nm compared with 193 nm, at which these matrices ablate poorly, similar to other challenging materials such as gypsum and barite. In these materials, 193 nm laser radiation penetrates substantially deeper than 157 nm radiation,[56] which can lead to uncontrolled ablation. Moreover, studies have indicated that 157 nm ablation produces reduced elemental and isotopic fractionation relative to longer wavelengths.[57,58] This is advantageous for Rb–Sr geochronology given the strong matrix-dependent fractionation of Rb and Sr combined with the lack of suitable matrix-matched secondary reference materials.

2. Materials and methods

2.1 Materials

All samples originated from the Morsleben site (NE, Germany), located within the Allertal zone, a NW–SE trending fault system. Upper Permian (Zechstein) salt migrated into these faults in several phases from the Mesozoic to the Cenozoic and subsequently experienced intense deformation.[59–61] The site was used for the disposal of low-to-intermediate-level radioactive waste

between 1971 and 1998. Preparations for the closure of this repository are underway.

Two sylvite samples (P3 and P10) and one carnallite sample (CT3) were investigated. These had been sampled at and near the "Bunte First", an extensive vein mineralization (1 m-to-10 m scale) hosted within fractured anhydrite rocks.[62] This style of mineralization indicates a secondary and, therefore, younger origin of the minerals compared with the Zechstein depositional age. The assemblage comprises carnallite, sylvite, polyhalite, and commonly purple-to-dark-blue halite. Samples were transported in sealed plastic bags to the University of Frankfurt. They were placed in a desiccator on the same day to minimize alteration due to exposure to atmospheric humidity. A few weeks later, all samples were cut to size using a rotating steel saw without water cooling. The resulting pieces were then embedded in a 1-inch epoxy resin block, impregnated several times with epoxy and dry-polished using silicon carbide (SiC) abrasive papers (400 up to 2000 grit). The final epoxy mounts were sealed in plastic bags and placed in a desiccator. For transport from Goethe Universität Frankfurt to the BGR Hanover, the bags were additionally filled with hygroscopic silica gel. Reflected light images of the mounts are provided in Fig. 1. Further description of the samples is given in the SI.

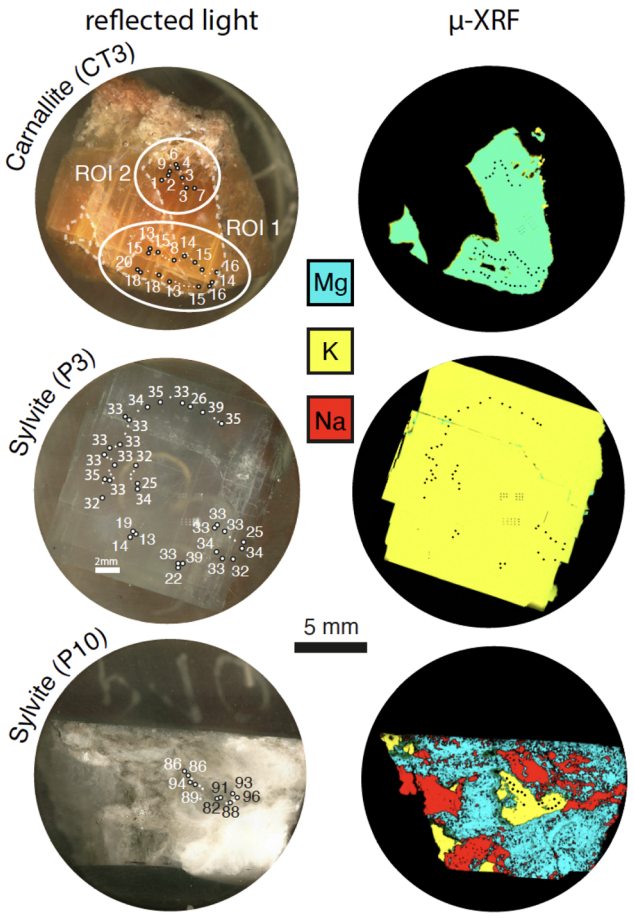

Fig. 1 Reflected-light images and μ-XRF element maps of investigated K-salt samples. Sample CT3 consisted of pure carnallite ($KMgCl_3 \cdot 6H_2O$), whereas sample P3 was composed of pure sylvite (KCl). Sample P10 represents an intergrowth of sylvite, halite (NaCl), and kieserite ($MgSO_4 \cdot H_2O$). Carnallite is depicted in cyan, reflecting its composition as a mixed potassium-magnesium chloride; the color results from the combination of yellow (K) and blue (Mg). White spots mark the locations of LA-ICP-MS/MS. Selected spots are labelled with corresponding Rb–Sr ages. The full set of analytical spots is shown in SI Fig. S1.

2.2 Reflected light and electron microscopy

We tested the ablation behavior of K-salt samples using laser wavelengths of 193 nm and 157 nm. High-resolution secondary electron (SE) images of the ablation pits (Fig. 2) were acquired using a field emission scanning electron microscope (Quanta 650F; FEI) at the BGR Hanover (pressure = 0.6 mbar, accelerating voltage = 15 kV, working distance = 13.6 mm). Additionally, the depth of the ablation pits was determined under reflected light using an optical digital microscope (VHX; Keyence) at Goethe University Frankfurt.

2.3 Micro-energy-dispersive X-ray fluorescence microscopy (μ-XRF)

Mineralogy and homogeneity on a micro-scale were verified by μ-XRF using the M4 Tornado Plus (Bruker Nano) system at the BGR Hanover. The device operates with a Rh tube at 50 kV and 600 μA with a spot size of ~20 μm at 17.4 keV focused by a polycapillary lens.[63] The sample chamber is evacuable to 2 mbar, thereby enhancing the limit of detection (LOD) and permitting measurement of elements as light as carbon. Mounts were measured with a step size of 20 μm and a dwell time of 20 ms per pixel. Measurement data were analyzed with M4 Tornado software and the results are presented as element distribution maps with element intensities in false colors. Element quantification was done using the standard-less fundamental parameter method.

2.4 *In situ* Rb–Sr dating and trace element analyses by LA-ICP-MS/MS

Single-spot *in situ* Rb–Sr dating and trace element analyses of sylvite and carnallite were performed at the FIERCE Laboratory of Goethe University Frankfurt using a reaction-cell LA-ICP-MS/MS system and overall followed the method described by Kutzschbach *et al.* in 2026.[64] An 8900 spectrometer (Agilent Technologies) was coupled to a custom-built dual-wavelength (157 and 193 nm) LA system.[56] Specifically, the analytical setup comprised a RESOlution-SE laser ablation system (Applied Spectra, USA) equipped with an S-155 laser ablation cell (Laurin Technic, Australia) and two excimer lasers that in part had separate beam-delivery systems: ExciStar 500 (193 nm) and Coherent COMPex F2 (157 nm). Both lasers deliver beams with a higher-order super gaussian intensity distribution but varying pulse length of 7 ns (193 nm) and 20 ns (157 nm). The latter was used for all analytical measurements. Spot sizes of 104 μm, a fluence of 2.5 J cm^{-2} and a laser repetition rate of 10 Hz were applied. For LA-ICP-MS/MS coupling, a "squid" signal-smoothing device (Laurin Technic)[65] was employed to improve signal stability. Ablation took place in He (0.3 l min^{-1}) to which Ar (0.95 l min^{-1}) + N_2 (3.5 ml min^{-1}) was added from the top of the ablation funnel, whose stepwise geometry prevents He–Ar–N_2 mixing directly at the ablation site. Pure (99.999%) nitrous oxide (N_2O) at a flow rate of 0.193 ml

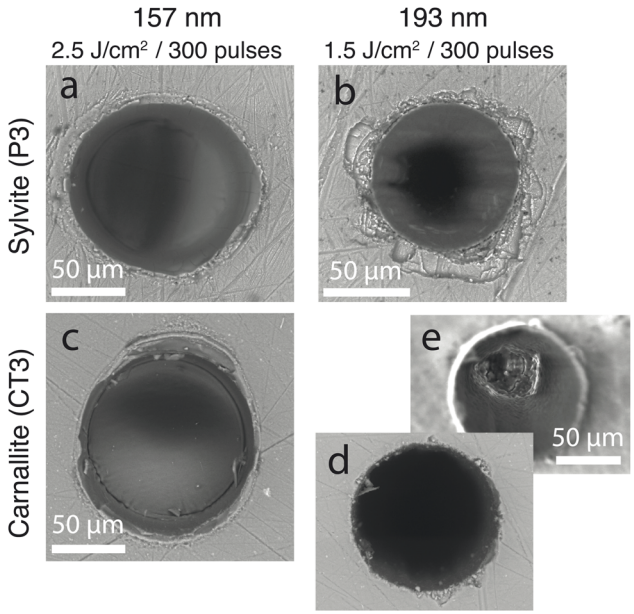

Fig. 2 Environmental secondary electron images of ablation pits produced after 300 laser pulses at wavelengths of 157 nm (2.5 J cm^{-2}) and 193 nm (1.5 J cm^{-2}). (a) and (b) show concentric backscattered electron images of sylvite P3. At 193 nm, pronounced chipping was observed at crater edges, whereas ablation at 157 nm produced pits characterized by smooth crater walls and bottoms. (c) and (d) show concentric backscattered electron images of carnallite CT3. For CT3, ablation at 193 nm was characterized by markedly higher ablation rates and crater bottoms exhibiting pronounced surface roughness and strong tapering with depth, as further illustrated in the large-field secondary electron image in (e). In contrast, ablation at 157 nm resulted in smooth, well-defined ablation pits with an approximately cylindrical geometry.

min^{-1} gas was used as a reactive cell gas to resolve the isobaric interference of ^{87}Rb and ^{87}Sr through measuring ^{86}Sr, ^{87}Sr, and ^{88}Sr as mass-shifted $^{86/87/88}Sr^{16}O^+$ (70 ms per sweep each). Rb was acquired as ^{85}Rb 'on-mass' (50 ms per sweep) to avoid interference of residual on-mass ^{87}Sr with ^{87}Rb. The formation of RbO^+ was negligible (zero counts per second (cps) was recorded at $m/z = 101$). Moreover, the following nuclides were recorded (brackets show dwell times in ms): ^{7}Li (5), ^{11}B (5), $^{23}Na^{16}O$ (5), ^{24}Mg (2), ^{27}Al (2), $^{28}Si^{32}O_2$ (5), $^{34}S^{16}O$ (2), $^{35}Cl^{16}O$ (10), ^{41}K (2), ^{43}Ca (2), ^{79}Br (10), ^{81}Br (10), ^{127}I (10), ^{133}Cs (5), ^{137}Ba (5), ^{208}Pb (2), and ^{238}U (2). The sweep time was 382 ms. The following reference materials were used: NIST610, NIST612, BHVO-2G, GSD-1F, GSE-1G, CGL026 halite (which was pressed into an ablatable pellet using a hydraulic press), SagaB biotite, SagaB alkali feldspar, 98 973 muscovite and Phalaborwa biotite.[66–71] More detailed information regarding the ICP-MS/MS and laser settings are compiled in Table S1.

Rb–Sr isotopic and chemical data were reduced using LADR software.[72] Isotope ratios were calculated as inverse ratios ($^{87}Rb/^{87}Sr$ and $^{86}Sr/^{87}Sr$) based on a ratio-of-means approach and discarding the first 3 s of the signal (rise time and surface contamination). Whenever conventional isotope ratios are reported, they are derived from the processed inverse ratios rather than being calculated independently from raw data.

Gas-blank and drift-corrected $^{87}Rb/^{87}Sr$ were corrected for mass bias using NIST610 ($^{87}Rb/^{87}Sr = 3.3638 \pm 0.0071$; $^{86}Sr/^{87}Sr = 1.409048 \pm 0.000036$) and $^{86}Sr/^{87}Sr$ ratios using NIST612 ($^{87}Rb/^{87}Sr = 1.633 \pm 0.021$; $^{86}Sr/^{87}Sr = 1.410312 \pm 0.000040$); $^{86}Sr/^{87}Sr$ from the work of Woodhead and Hergt in 2001;[66] $^{87}Rb/^{87}Sr$ from certified Rb/Sr concentrations.[67,68] The pulse/analog (P/A) factor was tuned once at the beginning of the session in MS/MS mode[64] and the P/A crossover was set to 10^7 cps multiplied by the P/A factor, with the latter being ~0.183 for $^{86+16}Sr$, ~0.177 for $^{87+16}Sr$, ~0.185 for $^{88+16}Sr$ and ~0.188 for ^{85}Rb. However, we observed significant drift of the P/A factor (up to 0.4%/h but varying from session to session), so we applied P/A-matched calibration of $^{86}Sr/^{87}Sr$ and $^{87}Rb/^{87}Sr$ ratios. NIST SRM612 was used as the primary reference material for the calibration of $^{86}Sr/^{87}Sr$ ratios using $^{86+16}Sr$ and $^{87+16}Sr$, which were both recorded in pulse mode similar to all samples and secondary reference materials except for CGL analysis #001 (here both $^{86+16}Sr$ and $^{87+16}Sr$ in analog mode) and BHVO-2G analysis #001-003 (here $^{86+16}Sr$ in analog). NIST SRM610 had both $^{86+16}Sr$ and $^{88+16}Sr$ in analog mode and $^{87+16}Sr$ in pulse mode and, hence, was not an alternative for calibration. Due to the P/A bias, these analyses were not considered further. In contrast, the $^{87}Rb/^{87}Sr$ ratios were calibrated using NIST SRM610, because ^{85}Rb was consistently measured in analog mode, whereas $^{87+16}Sr$ was measured in pulse mode. An exception was applied to SagaB alkali feldspar analyses #012 and #019-021, in which ^{85}Rb was measured in pulse mode; for these analyses, $^{87}Rb/^{87}Sr$ ratios were calibrated using NIST SRM612. This approach ensured appropriate P/A matching between samples and reference materials in all cases. Downhole fractionation (DHF) of $^{87}Rb/^{87}Sr$ ratios over the ablation interval was modelled with a cubic polynomial.

Matrix-corrected $^{87}Rb/^{87}Sr$ ratios were obtained using the expected age (2058.2 ± 7 Ma)[71] and measured isochron age of the Phalaborwa RM (1966.4 ± 9.1 Ma) and the following equation:

$$\left(^{87}Rb/^{87}Sr\right)_{\text{matrix corrected}} = \left(^{87}Rb/^{87}Sr\right) \cdot \frac{e^{\left[\left(RM_{age,measured} * \lambda\right)-1\right]}}{e^{\left[\left(RM_{age,expected} * \lambda\right)-1\right]}} \quad (1)$$

With λ being the ^{87}Rb decay constant.[73] External uncertainties (*i.e.*, the uncertainty of λ, NIST isotope ratios and the Phalaborwa expected age and its reproducibility) were added to the internal uncertainty in quadrature to obtain the fully propagated uncertainty. No statistically significant excess scatter neither within-run nor long-term was detected for NIST610 isotope ratios. For the isochron ages of reference materials, the internal uncertainty was constrained by the uncertainty resulting from the isochron fit. Model single-spot ages were calculated for K-salts by applying an initial $^{87}Sr/^{86}Sr$ isotope ratio of 0.75 ± 0.05. Here, the uncertainty introduced by the uncertainty of the initial $^{87}Sr/^{86}Sr$ isotope ratio was included in the fully propagated uncertainty of single spot ages. Isochron ages and single-spot ages were calculated using IsoplotR.[74]

The chemical composition was determined through calibration with NIST610 for Li, B, Na, Mg, Al, Si, S, K, Ca, Cs, Ba, Pb

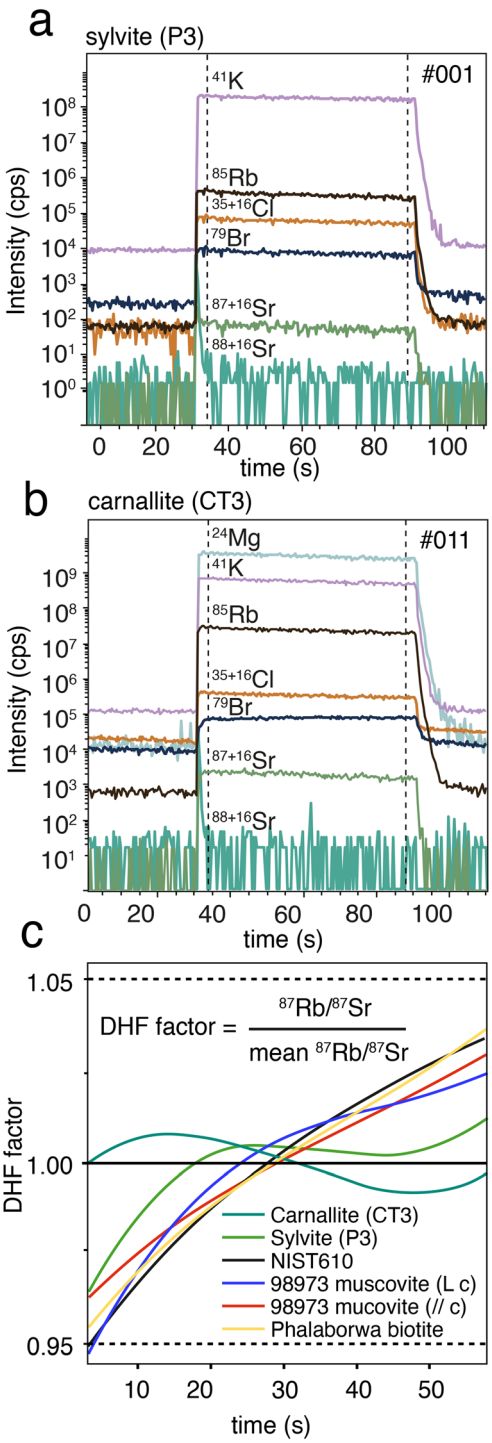

Fig. 3 LA-ICP-MS/MS signals acquired during static spot ablation of (a) sylvite P3 (spot #001) and (b) carnallite CT3 (spot #011) using the 157 nm laser (2.5 J cm^{-2}, 10 Hz, 60 s). The interval selected for quantification (dotted vertical lines) excluded the first 3 s to avoid contributions from surface contamination, which is indicated by increased ^{88}Sr concentrations at the beginning of the signal. After the first few laser pulses, the ^{88}Sr signal intensity remained close to that of the gas blank, whereas ^{87}Sr consistently was significantly above blank levels, suggesting that nearly all Sr present was derived from radiogenic ingrowth. Moreover, the smoothly declining Sr signal argued against Sr being hosted in (fluid) inclusions. Note the progressive accumulation of Br during the ablation of carnallite. (c) Downhole fractionation patterns for sylvite and carnallite compared with those of analyzed reference materials.

and U as the primary reference material. The halogens Cl, Br, and I were calibrated based on GSE-1G applying the values determined by the noble gas method published by Marks *et al.* in 2017.[75] All mica RM, SagaB alkalifeldspar, BHVO, GSD-1G and NIST612 were normalized using Si as an internal standard.[69,71] CGL026 was normalized using Na as an internal standard. All sylvite and carnallite analyses were normalized to K assuming stoichiometric K concentrations. CGL026 was normalized using Na as an internal standard. All sylvite and carnallite analyses were normalized to K assuming stoichiometric K concentrations of 52.45 wt% and 14.07 wt%, respectively.

3. Results and discussion

3.1 Ablation behavior at 157 nm

We evaluated the ablation characteristics of carnallite and sylvite by imaging the resulting crater pits at 193 nm (spot diameter of 80 μm and 1.5 J cm^{-2}) and 157 nm (spot diameter of 104 μm and 2.5 J cm^{-2}) wavelengths using secondary electron microscopy (Fig. 2). Craters generated at 157 nm displayed smooth and well-defined edges, whereas ablation at 193 nm resulted in pronounced chipping and irregular crater margins, indicating less controlled ablation behavior. Owing to the more stable ablation and significantly lower ablation rates, all subsequent analyses were, therefore, performed using the 157 nm wavelength. The resulting signals were smooth (Fig. 3) with low RSD% values (*e.g.*, ~1% for $^{24}Mg/^{41}K$ and $^{85}Rb/^{41}K$ and ~3.5% for $^{87}Sr/^{41}K$ in carnallite). Normalization to the internal standard (^{41}K) was applied to account for the overall downhole decrease in sensitivity, which is commonly observed during static spot ablation.

In addition to SEM, the crater depth and associated average per pulse ablation rate of carnallite, sylvite, NIST610 and the mica RM were determined using an optical digital microscope (VHX; Keyence). For sylvite even at relatively low fluences of 1.5 J cm^{-2}, the average ablation rate at 193 nm was ~700 nm per pulse, whereas at 157 nm a ~30% lower ablation rate of ~500 nm per pulse was obtained, despite the higher fluence at 157 nm of 2.5 J cm^{-2}. For carnallite, the difference in ablation rate between the two wavelengths was even more pronounced. At 157 nm and a fluence of 2.5 J cm^{-2}, an ablation rate of ~400 nm per pulse was obtained. In contrast, at 193 nm and a fluence of 1.5 J cm^{-2}, the resulting craters were too deep to bring their bottom into focus. Based on our experience, this indicated crater depths exceeding ~300 μm, corresponding to ablation rates of ≥1 μm per pulse. The large depth of CT3 craters is also illustrated in Fig. 2e. The high ablation rates at 193 nm were attributed to the lower threshold fluence and greater absorption depth for K-salts at 193 nm,[56] and would lead to rapidly increasing ablation depth during analyses, in turn leading to undesirably high DHF and overall reduction of aerosol transport. For NIST610 and the mica RM, average ablation rates of ~100 and ~80 nm were determined at 157 nm (2.5 J cm^{-2}) and 193 nm (1.5 J cm^{-2}), respectively. At a given wavelength, the difference in ablation rates between these matrices was not significant within the measurement uncertainty (~10%, 2SD).

3.2 Rb–Sr downhole fractionation

In contrast to the downhole fractionation (DHF) behavior of the mica reference material (RM), which closely followed that of NIST 610 and was characterized by a monotonically increasing $^{87}Rb/^{87}Sr$ ratio over the ablation interval, the wavy DHF patterns observed in carnallite and sylvite differed markedly. These K-bearing salts exhibited a 1–3% increase in $^{87}Rb/^{87}Sr$ during the first third of the ablation, followed by a 1–2% decrease in the second third, and a renewed increase of ~1% in the final third. Importantly, the overall magnitude of DHF in carnallite and sylvite was lower than that observed for NIST 610 and the mica RM, with maximum fractionation of ~1% for carnallite and ~3% for sylvite, compared with values of up to ~5% for the reference materials. This was remarkable considering the ~5-times higher ablation rates obtained for the K-salts compared with, for example, the mica RM (see Section 3.1) because higher aspect ratios (depth/width) generally promote stronger DHF. Consequently, no DHF correction was applied to K-salt analyses because application of a NIST 610-based DHF correction would result in overcorrection of the measured $^{87}Rb/^{87}Sr$ ratios. In contrast, NIST 610 was used for downhole correction of all reference materials, resulting in improved precision of the $^{87}Rb/^{87}Sr$ ratios (*e.g.*, the mean precision of the 98 973 muscovite RM improved from 0.72% to 0.62%). A constant ablation interval was maintained for all reference materials and for the vast majority of K-salt analyses. Ablation intervals were subdivided only if compositional variations within a single interval significantly exceeded analytical uncertainty and residual downhole bias, indicating multiple age domains (*e.g.*, carnallite analysis #005: 14.6 ± 0.41 Ma and 5.8 ± 0.22 Ma) (Table S1). In other instances, ablation intervals had to be shortened to avoid mixed analyses, such as the complex sylvite–halite–kieserite mixtures in sample P10.

It is important to note that omitting DHF corrections does not affect accuracy if the same ablation interval is used for both samples and RM, but it does lead to reduced precision. If, however, the ablation interval differs from that of the primary RM, a systematic bias is introduced; based on the DHF curves (Fig. 3), this bias was not expected to exceed 3% in case of K-salts.

3.3 Rb/Sr isotope ratios, ages and elemental chemistry of K-salt minerals

The sample-specific LOD was calculated following the approach of Longerich *et al.* in 1996.[76] The mean LOD was <0.5 ng g^{-1} for Sr and <0.7 ng g^{-1} for Rb. In sylvite and carnallite, non-radiogenic ^{86}Sr and ^{88}Sr were frequently below the (nominal) LOD. In these cases, the corresponding values were replaced by LOD/$\sqrt{2}$ following the approach of Frenzel detailed in 2023.[77] In contrast, ^{87}Sr was much more abundant and reached a mean concentration of 5–6 ng g^{-1} in CT3 and 17–39 ng g^{-1} in sylvites P3 and P10, respectively. Given the high Rb concentrations of 330–340 μg g^{-1} in CT3 carnallite and 46–110 μg g^{-1} in P3 and P10 sylvites, virtually all the measured ^{87}Sr (98.5–99.6%) was attributable to radiogenic ingrowth. Single-spot Rb–Sr analyses of carnallite CT3 yielded extremely high $^{87}Rb/^{86}Sr$ ratios of the order ~4 × 10^5 to ~1.2 × 10^7, reflecting the strongly Rb-enriched and common Sr-poor carnallite chemistry. Corresponding, $^{87}Sr/^{86}Sr$ ratios were highly radiogenic, ranging from ~5 to 2260. Sylvite samples P3 and P10 displayed increased but slightly less extreme $^{87}Rb/^{86}Sr$ ratios compared with carnallite. In sylvite P3, $^{87}Rb/^{86}Sr$ ratios ranged from ~1.2 × 10^5 to ~2.3 × 10^6, whereas sylvite P10 exhibited lower and more restricted ratios between ~3 × 10^4 and ~1.5 × 10^5. Corresponding $^{87}Sr/^{86}Sr$ ratios in P3 ranged from ~50 to ~800 and from ~40–160 in P10.

Individual $^{87}Sr/^{86}Sr$ analyses were characterized by relatively poor precision, with 2σ uncertainties ranging from ~6 to ~250%, which was attributed to the extremely low abundance of non-radiogenic Sr, commonly close to or below the LOD.

Model single-spot ages were calculated applying an initial $^{87}Sr/^{86}Sr$ ratio of 0.75 with a conservatively enlarged uncertainty of ±0.5. This range was selected to encompass the $^{87}Sr/^{86}Sr$ ratio of 0.70676–0.70776 reported for Permian seawater,[78] reflecting Sr incorporation during primary sedimentation, while also allowing for the introduction of additional radiogenic ^{87}Sr during diagenesis, fluid interaction and metamorphic overprint. However, given the radiogenic nature of the investigated K salts, the influence of the assumed initial Sr isotopic composition on the resulting Rb–Sr ages was negligible.[79] To illustrate this insensitivity, an intentionally extreme (and entirely implausible) initial $^{87}Sr/^{86}Sr$ ratio of 2.7 ± 2.0 was tested. Even under this extreme assumption, the single-spot age uncertainty increased by only ~0.13%, and the mean age shifted by ~1.1% towards younger values relative to the chosen ratio of 0.75 ± 0.5. The uncertainty of the latter ratio contributed only an additional ~1.2 × 10^{-5}% to the total single-spot age uncertainty budget, which amounted to a mean relative 2σ uncertainty of ~3% (Fig. 4 and Table S1). Previous analyses of Rb–Sr ID-TIMS performed on carnallite have yielded an age precision of 1–2% (2 RSD; see SI Table S2) per analysis. This difference in precision is modest, despite the substantially higher precision of Sr isotope ratio measurements obtained by ID-TIMS (tens of parts per million) (SI Table S2) compared with LA-ICP-MS/MS (tens of percent) (SI Table S1). The reason is that, at such extreme Rb/Sr ratios, age precision is dominated by the uncertainty in the Rb/Sr ratio. This uncertainty is of similar magnitude for LA-ICP-MS/MS (~3%) and ID-TIMS (1–2%).

Single-spot Rb–Sr ages of carnallite CT3 and sylvite samples P3 and P10 define distinct age distributions. Carnallite CT3 comprises two spatially and geochemically distinct regions of interest (ROI1: analyses #001 to #038; ROI2: analyses #039 to #050), represented by spot clusters sampled ~1 cm apart (Fig. 1). ROI1 yielded older single-spot ages ranging from ~5.8 to ~21.6 Ma, whereas ROI2 defined a younger population between ~0.7 and ~8.8 Ma. Adaptive kernel density estimates (KDE) of CT3 single-spot ages reveal a clear bimodal distribution with modes at ~4 Ma and ~14 Ma (Fig. 4), consistent with the presence of two age populations. This subdivision into ROIs was supported by distinct trace-element compositions, particularly regarding B and Cs concentrations. ROI1 was characterized by a mean B concentration of 0.29 ± 0.03 ppm (2SE) and mean Cs concentration of 12.09 ± 0.13 ppm (2SE), whereas

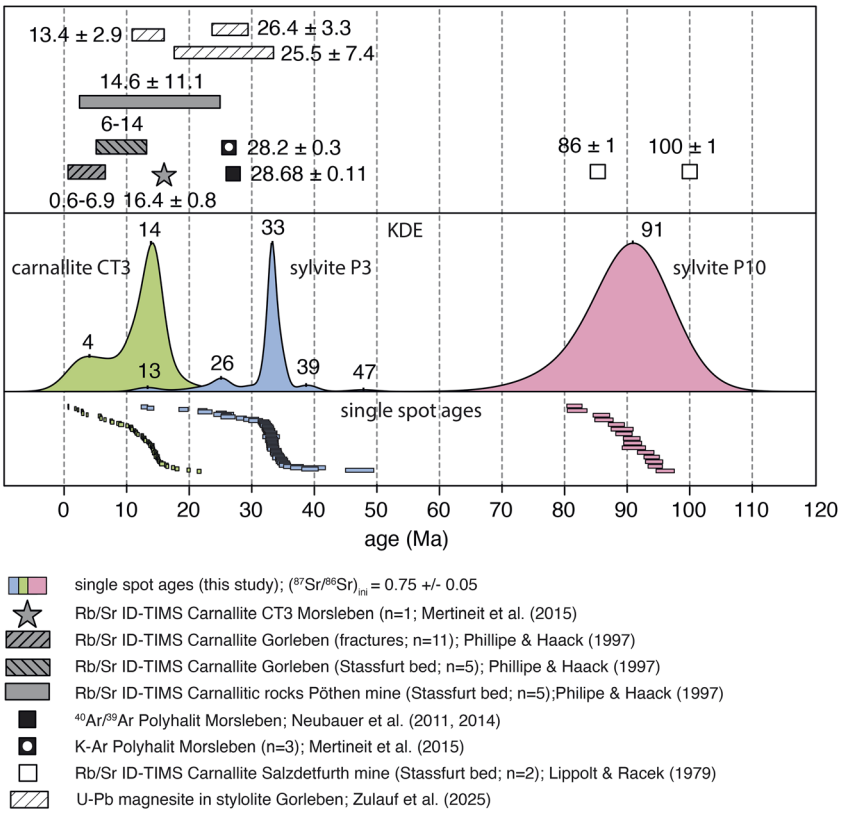

Fig. 4 Compilation of single-spot Rb–Sr ages obtained for the three investigated potassium salts together with the resulting adaptive kernel density estimate (KDE). The width of the bars denotes the 2 s uncertainty. All single-spot ages are also compiled in Table S1. The top part of the figure shows available literature data for salt minerals of Morsleben and other German salt mines located in the proximity. The latter have been recalculated using the ^{87}Rb decay constant of Villa *et al.*[73] (2015); see Table S2.

ROI2 exhibited an approximately twofold higher mean B concentration of 0.64 ± 0.03 ppm (2SE) and slightly lower mean Cs concentration of 11.57 ± 0.18 ppm (2SE) (Table 1). Sylvite P10 displayed a unimodal age distribution with a KDE mode centered at ~91 Ma. In contrast, sylvite P3 exhibited more complex age systematics, characterized by a dominant KDE mode at ~33 Ma, subordinate modes at ~26 Ma and ~39 Ma, two analyses yielded ages around ~13 Ma, and one analysis recorded an older age of ~47 Ma. No correlation was detected between trace-element chemistry and Rb–Sr single-spot ages for sylvite P10 or P3.

3.4 Accuracy of the single-spot ages of sylvite and carnallite

No matrix-matched secondary reference material was available to directly assess the accuracy of the Rb–Sr ages obtained for K-salt minerals. Nevertheless, the ages obtained for the mica reference materials muscovite 98 973 (265.5 ± 2.3 Ma with *c*-axis oriented perpendicular to the incident laser beam, and 268.9 ± 2.1 Ma with *c*-axis parallel to the incident laser beam), as well as for the SagaB alkali feldspar (295.5 ± 6.7 Ma), agreed well with their expected ages (98 973: 266.8 ± 1.6 Ma; SagaB alkali feldspar: 295.4 ± 1.4 Ma; ID-TIMS by Kutzschbach and Glodny in 2024).[71] The SagaB biotite yielded a slightly older age than expected (300.2 ± 2.6 Ma *vs.* 295.4 ± 1.4 Ma)[71] although the resulting bias was limited to ~1%.

It is noteworthy that the Rb–Sr elemental fractionation at 157 nm was substantially smaller than that typically observed at 193 nm. For example, the uncorrected age obtained for the matrix reference material Phalaborwa biotite at 157 nm was 1966.4 ± 9.1 Ma, compared with its expected age of 2058.2 ± 7 Ma,[71] corresponding to a matrix-bias of only ~5%. In contrast, matrix biases at 193 nm were commonly significantly larger, typically on the order of ~10%.[64,71,80–83] Consequently, although a matrix-matched reference material for K salts is lacking, any systematic age offset associated with Rb/Sr elemental fractionation at 157 nm is expected to be much smaller than at 193 nm.

Further support of the obtained K-salt ages comes from the available, albeit limited, literature data. Age distributions compatible with the bimodal Rb–Sr age distribution observed for CT3 carnallite (KDE modes at ~14 Ma and ~4 Ma) have been reported from the nearby Gorleben salt dome, which shares a similar genetic and tectonic evolution with the one in Morsleben. There, Rb–Sr ID-TIMS of carnallite from the Permian Straßfurth bed yielded model ages between 6 and 14 Ma (assuming an initial ^{87}Sr/^{86}Sr of 0.707, typical of Permian seawater), interpreted as partial isotopic resetting due to ^{87}Sr loss induced by recrystallization associated with diapiric movement.[30] Notably, undeformed primary carnallite from the Pöthen mine (Thuringia, Germany) had a comparable reset age of 14.6 ± 11.1 Ma (isochron age recalculated using the ^{87}Rb decay constant of Villa *et al.* in 2015),[73] indicating that isotopic

Table 1 Mean trace element concentration and percentage of radiogenic ^{87}Sr of investigated K-salts, obtained using LA-ICP-MS/MS and μ-XRF

	CT3				P3		P10	
	ROI1		ROI2					
Element	Mean	2 SE (abs)	Mean	2 SE (abs)	Mean	2 SE (abs)	Mean	2 SE (abs)
Li	0.012	0.0055	<DL		0.015	0.002	0.048	0.015
B	0.64	0.027	0.29	0.032	0.79	0.13	0.39	0.089
Na	<DL		<DL		8700	830	14 000	2500
Mg	92 000	350	91 000	1100	1.4	2	8.4	12
Al	0.19	0.32	0.041	0.0031	0.049	0.0036	0.06	0.023
Si	51	1.6	49	1.4	85	1.3	100	1.6
S	65	2.7	62	3.9	68	1.9	84	11
Ca	<DL		<DL		<DL		<DL	
Rb	330	4.6	340	2.9	46	0.69	110	1.3
Rb (μXRF)	356	1.5	346	2	43	0.5	65	2.5
Br (μXRF)	2718	4	2629	5.4	1067	2.6	3074	17.1
^{86}Sr	0.00011	0.00014	0.000051	0.000033	0.000034	0.0000079	0.00048	0.00013
^{87}Sr	0.017	0.0011	0.0054	0.0019	0.006	0.00045	0.039	0.00096
^{88}Sr	0.00075	0.0011	0.00019	0.000087	0.00011	0.000028	0.0036	0.00091
Cs	11.6	0.18	12.1	0.13	0.0079	0.0006	0.014	0.00089
Ba	0.31	0.16	0.13	0.076	0.27	0.033	0.35	0.1
Pb	0.0024	0.0025	0.0018	0.00063	1	0.37	0.013	0.018
U	0.12	0.00021	0.12	0.085	0.13	0.093	0.13	0.002
$^{87}Sr^*$ (%)[a]	99.5		98.5		99.6		99.1	

[a] Data are in μg g^{-1}, DL = detection limit calculated following the approach of Longerich *et al.* (1996),[76] For assignment of ROI1/ROI2, compare Fig. 1, Complete table containing individual analyses is provided in Table S1. Amount of radiogenic ^{87}Sr calculated assuming an initial (non-radiogenic) $^{87}Sr/^{86}Sr$ ratio of 0.72.

resetting was not exclusively controlled by deformation but likely involved temperature- or fluid-assisted processes. Philippe and Haack (1997)[30] also documented a younger generation of carnallite occurring as fracture fillings within a 50–80 m thick anhydrite unit that underwent brittle deformation during late Gorleben diapirism, yielding significantly younger ages of 0.6–6.9 Ma.

The distinct B and Cs concentrations associated with the two different age modes of CT3 suggested that the younger age population may have resulted from fluid-induced isotopic resetting, given that B and Cs are fluid-mobile elements. Accordingly, the observed geochemical differences between the ROIs are consistent with dissolution–reprecipitation or fluid-assisted recrystallization processes that could partially or fully reset the Rb–Sr system. Episodic fluid flow in the upper Cenozoic may have been associated with the Rhine rift system, which remained active throughout the Cenozoic until the present.[84] Moreover, a piece of CT3 carnallite was previously analyzed by ID-TIMS, yielding an age of 16.4 ± 0.8 Ma,[31] which overlaps with the range of single-spot ages obtained in the present study (0.7–21.6 Ma). However, considering the centimeter-scale age heterogeneity of CT3 revealed in our study, comparisons with age data derived from bulk samples are inherently limited.

The dominant age population of sylvite P3 at ∼33 Ma was close to the published $^{40}Ar/^{39}Ar$ ages of polyhalite (∼28 to 29 Ma)[19,20,31] It has been suggested that the formation or recrystallization of the latter is linked to tectonic processes associated with subsidence of the North German Basin.[31] Contemporaneous fluid activity during this tectonic phase is documented by U–Pb ages of stylolitic magnesite formed by incongruent dissolution–reprecipitation of anhydrite within the Gorleben salt dome (25.5 ± 7.4 Ma, 26.4 ± 3.3 Ma, and 13.4 ± 2.9 Ma).[33]

The dominant age mode of P10 sylvite at ∼91 Ma closely coincided with the Rb–Sr ID TIMS ages of carnallite from the Salzdetfurth mine located only ∼100 km from Morsleben (86 ± 1 and 100 ± 1 Ma).[28] These ages may be linked to the onset of late Cretaceous intraplate contraction in central Europe, which is a result of a fundamental change in the relative plate motion between Africa and Europe at ∼90 Ma.[85] This tectonic reorganization is characterized by widespread basement thrusting and foreland deformation, and likely promoted enhanced fluid circulation and mineral reactions within the salt system. These phenomena provide favorable conditions for sylvite/carnallite formation and/or isotopic resetting at that time.

4. Conclusions

We demonstrated that *in situ* Rb–Sr geochronology of potassium-bearing evaporite minerals was feasible with sufficient precision using 157 nm laser ablation coupled with ICP-MS/MS. Compared with 193 nm radiation, the 157 nm wavelength provided significantly more stable and controlled ablation of sylvite and carnallite. The resulting single-spot ages revealed spatially heterogeneous age populations that may record multiple episodes of recrystallization and fluid-mediated isotopic resetting within the Morsleben salt system during Cretaceous and Cenozoic periods. These results highlight the potential of high-spatial-resolution Rb–Sr dating of K-salt minerals to directly constrain the tectonic and fluid-flow history of evaporite deposits. By providing insights into the timing and

extent of past fluid migration and deformation, such evaporite systems serve as natural experiments over geological timescales. Consequently, they improve predictions of the long-term geochemical stability of salt formations and provide valuable constraints for geological site assessments, particularly in the context of radioactive waste disposal, where safety must be demonstrated over timescales of up to hundreds of thousands of years. In Germany, for example, the considered assessment period is 1 000 000 years for high-level, heat-generating waste.

Conflicts of interest

There are no conflicts to declare.

Data availability

The data present in this article and further supplementary data are available through the Zenodo repository (https://doi.org/10.5281/zenodo.19608381).

Acknowledgements

This work was funded by a Deutsche Forschungsgemeinschaft (DFG) grant (project ID: 5387656229) awarded to MK. LA-ICP-MS/MS equipment funding was provided by a DFG Large Equipment Grant (INST 161/1073-1 FUGG) to WM. FIERCE is financially supported by the DFG (INST 161/921-1 FUGG, INST 161/923-1 FUGG) and received financial support from the Wilhelm and Else Heraeus Foundation, which is gratefully acknowledged. We sincerely thank Hartmut Blanke and Mario Patzschke (BGE) for their guidance during our visit to Morsleben in March 2025. Alexander Schmidt (GU) is acknowledged for technical support during LA-ICP-MS/MS. The comments of two journal reviewers helped to improve the clarity of our presentation and are gratefully acknowledged, as is the swift editorial handling throughout. This is FIERCE contribution no. 237

References

1 J. Winterle, G. Ofoegbu, R. Pabalan, C. Manepally, T. Mintz, E. Pearcy and R. Fedors, *Geologic disposal of high-level radioactive waste in salt formations*, Contract NRC-02-07-006, US Nuclear Regulatory Commission, 2012.

2 T. von Berlepsch and B. Haverkamp, Salt as a host rock for the geological repository for nuclear waste, *Elements*, 2016, **12**, 257–262.

3 J. D. O. Williams, J. P. Williamson, D. Parkes, D. J. Evans, K. L. Kirk, N. Sunny, E. Hough, E. Vosper and M. C. Akhurst, Does the United Kingdom have sufficient geological storage capacity to support a hydrogen economy? Estimating the salt cavern storage potential of bedded halite formations,*J. Energy Storage*, 2022, **53**, 105109.

4 J. Miocic, N. Heinemann, K. Edlmann, J. Scafidi, F. Molaei, and J. Alcalde, *Underground Hydrogen Storage: a Review*, Geological Society, London, Special Publications, 2023, pp. 73–86.

5 W. Liu, Q. Li, C. Yang, X. Shi, J. Wan, M. J. Jurado, Y. Li, D. Jiang, J. Chen, W. Qiao, X. Zhang, J. Fan, T. Peng and Y. He, The role of underground salt caverns for large-scale energy storage: A review and prospects, *Energy Storage Mater.*, 2023, **63**, 103045.

6 W. Liu, J. Chen, D. Jiang, X. Shi, Y. Li, J. J. K. Daemen and C. Yang, Tightness and suitability evaluation of abandoned salt caverns served as hydrocarbon energies storage under adverse geological conditions (AGC), *Appl. Energy*, 2016, **178**, 703–720.

7 J. Raymond, H. Langevin, F.-A. Comeau and M. Malo, Temperature dependence of rock salt thermal conductivity: Implications for geothermal exploration, *Renew. Energy*, 2022, **184**, 26–35.

8 J. Chang, Y. Qi, R. Yang and T. Hao, The self-healing property of rock salt damage in underground gas storage: A review, *Results Eng.*, 2025, **27**, 106098.

9 G. J. Orris, M. D. Cocker, P. Dunlap, J. C. Wynn, G. T. Spanski, D. A. Briggs and L. Gass, Potash: a global overview of evaporite-related potash resources, including spatial databases of deposits, occurrences, and permissive tracts, *Sci. Invest. Rep.*, 2014.

10 A. P. Dickin, *Radiogenic Isotope Geology*, Cambridge University Press, 2nd edn, New York, 2005.

11 J. Pilot and P. K. Blank, Ar-Bestimmungen von Salzgesteinen des Zechsteins, *Z. Angew. Geol.*, 1967, **13**, 661–662.

12 N. C. Wardlaw, Carnallite-Sylvite Relationships in the Middle Devonian Prairie Evaporite Formation, Saskatchewan, *Geol. Soc. Am. Bull.*, 1968, **79**, 1273–1294.

13 D. G. Brookins, J. K. Register and H. W. Krueger, Potassium-argon dating of polyhalite in southeastern New Mexico, *Geochim. Cosmochim. Acta*, 1980, **44**, 635–637.

14 D. G. Brookins, H. W. Krueger and T. M. Bills, Rb-Sr and K-Ar analyses of evaporite minerals from southeastern New Mexico. Isochron/West, *Bull. Isot. Geochronol.*, 1985, **43**, 11–12.

15 H. J. Lippolt, S. Hautmann and J. Pilot, 40Ar/39Ar-Dating of Zechstein Potash salts: New constraints on the numerical age of the Latest Permian and the P-Tr boundary, *Terra Abstr.*, 1993, **5**, 591.

16 S. Halas, A. Wójtowicz and T. M. Peryt, K/Ar dates of some Miocene potash salts from Carpathian Foredeep, *Acta Geol. Hung.*, 1996, **39**, 64–67.

17 I. Léost, G. Fraud, M. M. Blanc-Valleron and J. M. Rouchy, First absolute dating of Miocene langbeinite evaporites by 40Ar/39Ar laser step-heating: [K2Mg2(SO4)3] Stebnyk mine (Carpathian Foredeep Basin), *Geophys. Res. Lett.*, 2001, **28**, 4347–4350.

18 A. Wójtowicz, S. P. Hryniv, T. M. Peryt, A. Bubniak, I. Bubniak and P. M. Bilanizhka, K/Ar dating of the Miocene potash salts of the Carpathian foredeep (West Ukraine): Application to dating of tectonic events, *Geol. Carpathica*, 2003, **54**, 243–249.

19 F. Neubauer, C. Leitner, A. Schorn, and J. Genser, Dating of sulphates and their deformation structures: preliminary results from German Zechstein and Austrian Haselgebirge,

Fragile Earth, Munich International Conference Abstracts with Programs, vol. 4, 2011.

20 F. Neubauer, A. Schorn, J. Genser, and C. Leitner, Ar-Ar dating of polyhalite and langbeinite in evaporite bodies, *Goldschmidt 2014 Abstracts*, 2014, p. 1789.

21 C. Leitner, F. Neubauer, J. Genser and M. Bernrolder, Dating of polyhalite: a difficult 40Ar/39Ar dating tool of diagenitic to very low-grade metamorphic processes, *Int. J. Earth Sci.*, 2022, **111**, 2037–2051.

22 N. I. Polevaya, N. E. Titov, V. S. Belayev and V. D. Sprintsson, Application of the Ca method in the absolute age determination of sylvite, *Geochemistry*, 1958, **8**, 897–906.

23 H. G. Wilhelm and W. Ackermann, Altersbestimmung nach der K-Ca-Methode an Sylvin des Oberen Zechsteins des Werragebietes, *Z. Naturforsch. A*, 1972, **27**, 1256–1259.

24 J. D. Obradovich, M. Tatsumoto, O. K. Manuel, H. Mehnert, M. Domenick, and T. K. Wildman, Ar and K-Ca dating of Sylvite from the Late Permian Salado Formation, New Mexico. Implications regarding Stability of Evaporite Minerals, *Abstracts Fifth International Conference on Geochronology, Cosmochronology, Isotope Geology*, Nikko National Park, Japan, 1982, pp. 283–284.

25 H. Baadsgaard, Rb-Sr and K-Ca isotope systematics in minerals from potassium horizons in the Prairie Evaporite Formation, Saskatchewan, Canada, *Chem. Geol.*, 1987, **66**, 1–15.

26 F. Henjes-Kunst, W. Prochaska, and M. Schramm, Application of the Sm-Nd isochron method to dating of evaporitic and hydrothermal carbonates, *Goldschmidt Conference Abstracts*, vol. 2008, 2008, p. A368.

27 F.-P. Oesterle and H. J. Lippolt, Isotopische Datierung der Langbeinitbildung in der Kalisalzlagerstätte des Fuldabeckens, *Kali Steinsalz*, 1975, **6**, 391–398.

28 H. J. Lippolt and I. Raczek, Cretaceous Rb-Sr Total Rock Ages of Permian Salt Rocks, *Naturwissenschaften*, 1979, **66**, 422–423.

29 S. Philippe and U. Haack, Rb-Sr study on langbeinite and other salt minerals from a Zechstein diapir in northern Germany, *Chem. Geol.*, 1995, **123**, 199–207.

30 S. Philippe and U. Haack, Rb-Sr Systematics in Carnallitites and Carnallitic Rocks from the German Zechstein, *Geol. Jahrbuch Reihe E Geophys.*, 1997, **57**, 3–21.

31 M. Mertineit, J. Hammer, and M. Schramm, Alterbestimmung von Kluftmineralisationen und Deformationsprozessen in Salinargesteinen, *Zwischenbericht 9Y3203000000*, BGR, Hannover, 2015.

32 A. Beranoaguirre, I. Vasiliev and A. Gerdes, In situ LA-ICPMS U-Pb dating of sulfates: applicability of carbonate reference materials as matrix-matched standards, *Geochronology*, 2022, **4**, 601–616.

33 G. Zulauf, A. Gerdes, D. Hezel, B. Hohlmeier, J. Linckens and M. Mertineit, Tectonic stylolites in anhydrite rock: Constraints on fluid-assisted deformation and isotopic ages of salt rocks(Gorleben salt dome, Germany), *SSRN*, 2025, DOI: 10.2139/ssrn.5929693.

34 J. Yi, C. L. Kirkland, J. Bourdet, M. Barham, M. Danišík, A. Feitz, P. W. Haines, B. McDonald, B. V. Ribeiro, E. Frery and C. Delle Piane, Taken with a grain of salt: Resolving evaporite stratigraphy through accessory mineral geochronology, *Earth Planet. Sci. Lett.*, 2025, **671**, 119616.

35 J. Yi, C. L. Kirkland, M. Barham, M. Danišík and A. Feitz, Accessory mineral dating of the Boree Salt in the Adavale Basin, Queensland, Australia, *J. Geol. Soc.*, 2025, **183**, jgs2025–jgs2171.

36 R. D. Shannon, Revised ionic radii and systematic studies of interatomic distances in halides and chalcogenides, *Acta Crystallogr. A*, 1976, **32**, 751–767.

37 T. M. Harrison, J. Célérier, A. B. Aikman, J. Hermann and M. T. Heizler, Diffusion of 40Ar in muscovite, *Geochim. Cosmochim. Acta*, 2009, **73**, 1039–1051.

38 A. Scharf, M. R. Handy, S. M. Schmid, S. Favaro, S. Masafumi, R. Schuster and K. Hammerschmidt, Grain-size effects on the closure temperature of white mica in a crustal-scale extensional shear zone - implications of in situ 40Ar/39Ar laser-ablation of white mica for dating shearing and cooling (Tauern Window, Easter Alps), *Tectonophysics*, 2016, **674**, 210–226.

39 J. W. Purdy and E. Jäger, K-Ar ages on rock-forming minerals from the central Alps, *Mem. Ist. Geol. R. Univ. Padova*, 1976, **30**, 1–31.

40 R. Cliff, Isotopic dating in metamorphic belts, *J. Geol. Soc.*, 1985, **142**, 97–110.

41 R. A. Cliff, Rb-Sr dating of white mica – new potential in metamorphic geochronology, *Abstracts ICOG 8*, U.S. Geological Survey Circular, vol. 1107, 1994, p. 62.

42 A. Steck and J. C. Hunziker, The Tertiary structural and thermal evolution of the Central Alps - compressional and extensional structures in an orogenic belt, *Tectonophysics*, 1994, **238**, 229–254.

43 I. M. Villa, Isotopic closure, *Terra Nova*, 1998, **10**, 42–47.

44 J. Glodny, A. Kühn and H. Austrheim, Diffusion versus recrystallization processes in Rb-Sr geochronology: Isotopic relics in eclogite facies rocks, Western Gneiss Region, Norway, *Geochim. Cosmochim. Acta*, 2008, **72**, 506–525.

45 W. Gentner, R. Präg and F. Smits, Argonbestimmungen an Kalium-Mineralien II. Das Alter eines Kalilagers im Unteren Oligozän, *Geochim. Cosmochim. Acta*, 1953, **4**, 11–20.

46 W. Gentner, K. Goebel and R. Präg, Argonbestimmungen an Kalium-Mineralien III. Vergleichende Messungen nach der Kalium-Argon- und Uran-Helium-Methode, *Geochim. Cosmochim. Acta*, 1954, **5**, 124–133.

47 W. Müller, N. S. Mancktelow and M. Meier, Rb-Sr microchrons of synkinematic mica in mylonites: an example from the DAV fault of the Eastern Alps, *Earth Planet. Sci. Lett.*, 2000, **180**, 385–397.

48 D. Egli, W. Müller and N. Mancktelow, Laser-cut Rb-Sr microsampling dating of deformational events in the Mont Blanc-Aiguilles Rouges region (European Alps), *Terra Nova*, 2016, **28**, 35–42.

49 C. Li, Z. Chu, X. Wang, J. Guo and S. A. Wilde, Determination of 87Rb/86Sr and 87Sr/86Sr ratios and Rb-Sr contents on the same filament loading for geological samples by isotope dilution thermal ionization mass spectrometry, *Talanta*, 2021, **233**, 122537.

50 Z. Chu, T. Cui, T. C. Meisel, Y. Li, C. Li, L. Xu, Y. Yang and P. Peng, OU-9: A potential reference material with high 87Rb/86Sr and 87Sr/86Sr for data quality control and method validation in ID-MS Rb-Sr Geochronology, *Geostand. Geoanal. Res.*, 2025, 425–437.
51 T. Zack and K. J. Hogmalm, Laser ablation Rb/Sr dating by online separation of Rb and Sr in an oxygen-filled reaction cell, *Chem. Geol.*, 2016, **437**, 120–133.
52 K. J. Hogmalm, T. Zack, A. K.-O. Karlsson, A. S. L. Sjöqvist and D. Garbe-Schönberg, In situ Rb-Sr and K-Ca dating by LA-ICP-MS/MS: an evaluation of N2O and SF6 as reaction gases, *J. Anal. At. Spectrom.*, 2017, **32**, 305–313.
53 E. Bolea-Fernandez, S. J. M. Van Malderen, L. Balcaen, M. Resano and F. Vanhaecke, Laser ablation-tandem ICP-mass spectrometry (LA-ICP-MS/MS) for direct Sr isotopic analysis of solid samples with high Rb/Sr ratios, *J. Anal. At. Spectrom.*, 2016, **31**, 464–472.
54 L. J. Moens, F. Vanhaecke, D. R. Bandura, V. I. Baranov and S. D. Tanner, Elimination of isobaric interferences in ICP-MS using ion-molecule reaction chemistry: Rb/Sr age determination of magmatic rocks, a case study, *J. Anal. At. Spectrom.*, 2001, **16**, 991–994.
55 D. R. Bandura, V. Baranov, A. Litherland and S. D. Tanner, Gas-phase ion-molecule reactions for resolution of atomic isobars: AMS and ICP-MS perspectives, *Int. J. Mass Spectrom.*, 2006, **255–256**, 312–327.
56 T. Erhardt, A. Norris, R. Rittberger, M. Shelley, M. Kutzschbach, L. Marko, A. Schmidt and W. Müller, Rationale, design and initial performance of a dual-wavelength (157 & 193 nm) cryo-LA-ICP-MS/MS system, *J. Anal. At. Spectrom.*, 2025, **40**, 2857–2869.
57 R. E. Russo, X. L. Mao, O. V. Borisov and H. Liu, Influence of wavelength on fractionation in laser ablation ICP-MS, *J. Anal. At. Spectrom.*, 2000, **15**, 1115–1120.
58 P. Telouk, E. Rose-Koga and F. Albarède, Preliminary results from a new 157 nm laser ablation ICP-MS instrument: New opportunities in the analysis of solid samples, *Geostand. Newsl.*, 2003, **27**, 5–11.
59 J. Behlau and G. Mingerzahn, Geological and tectonic investigations in the former Morsleben salt mine (Germany) as a basis for the safety assessment of a radioactive waste repository, *Eng. Geol.*, 2001, **61**, 83–97.
60 G. Best and M. Zirngast, *Die strukturelle Entwicklung der exhumierten Salzstruktur "Oberes Allertal"*, Bundesanstalt für Geowissenschaften und Rohstoffe, Hannover, 2002, p. 114.
61 C. Brandes, C. Schmidt, D. C. Tanner and J. Winsemann, Paleostress pattern and salt tectonics within a developing foreland basin (north-western Subherzynian Basin, northern Germany), *Int. J. Earth Sci.*, 2013, **102**, 2239–2254.
62 J. Behlau, G. Mingerzahn and O. Bornemann, *Erarbeitung eines geologischen Lagerstättenmodells Morsleben*, Final Report, Bundesanstalt für Geowissenschaften und Rohstoffe, Hannover, 1997, p. 73.
63 W. Nikonow and D. Rammlmair, Risk and benefit of diffraction in Energy Dispersive X-Ray fluorescence mapping, *Spectrochim. Acta B Atom Spectrosc.*, 2016, **125**, 120–126.
64 M. Kutzschbach, J. Glodny, T. Erhardt and W. Müller, Rb-Sr age resetting by diffusion and neo-/recrystallization in amphibolite-facies metamorphic white mica revealed by micrometer scale LA-ICP-MS/MS mapping, *Chem. Geol.*, 2026, **712**, 123393.
65 W. Müller, M. Shelley, P. Miller and S. Broude, Initial performance metrics of a new custom-designed ArF excimer LA-ICPMS system coupled to a two-volume laser-ablation cell, *J. Anal. At. Spectrom.*, 2009, **24**, 209–214.
66 J. D. Woodhead and J. M. Hergt, Strontium, neodymium and lead isotope analyses of NIST glass certified reference materials: SRM 610, 612, 614, *Geostand. Newsl.*, 2001, **25**, 261–266.
67 S. A. Wise, and R. L. Watters, *Certificate of Analysis: Standard Reference Material 610*, National Institute of Standards and Technology, Gaithersburg, USA, 2012.
68 S. A. Wise, and R. L. Watters, *Certificate of Analysis: Standard Reference Material 612*, National Institute of Standards and Technology, Gaithersburg, USA, 2012.
69 K. P. Jochum, M. Willbold, I. Raczek, B. Stoll and K. Herwig, Chemical characterization of the USGS reference glasses GSA-1G, GSC-1G, GSD-1G, GSE-1G, BCR-2G, BHVO-2G and BIR-1G using EPMA, ID-TIMS, ID-ICP-MS and LA-ICP-MS, *Geostand. Geoanal. Res.*, 2005, **29**, 285–302.
70 M. Schramm and M. Mertineit, Stoffliche und mikrostrukturelle Untersuchungen zur Entstehung von Salzgesteinen in flacher Lagerung und in Salzstöcken. BGR Hannover, F+E Endlagerung, Abschlussbericht 9Y321502000, 2022, https://www.bgr.bund.de/DE/Themen/Endlagerung/Downloads/Endlagerforschung/2_Steinsalz/2022-07-25_mikrostrukturelle_untersuchungen_salz.pdf?__blob=publicationFile&v=5.
71 M. Kutzschbach and J. Glodny, LA-ICP-MS/MS-based Rb-Sr isotope mapping for geochronology, *J. Anal. At. Spectrom.*, 2024, **39**, 455–477.
72 A. Norris, and L. Danyushevsky, Towards Estimating the Complete Uncertainty Budget of Quantified Results Measured by LA-ICP-MS, *Goldschmidt*, Boston, 2018.
73 I. Villa, P. De Bièvre, N. Holden and P. Renne, IUPAC-IUGS recommendation on the half life of 87Rb, *Geochim. Cosmochim. Acta*, 2015, **164**, 382–385.
74 P. Vermeesch, IsoplotR: a free and open toolbox for geochronology, *Geosci. Front.*, 2018, **9**, 1479–1493.
75 M. A. W. Marks, M. A. Kendrick, G. N. Eby, T. Zack, T. T. F. Wenzel and Br Cl, I contents of reference glasses BHVO-2G, BIR-1G, BCR-2G, GSD-1G, GSE-1G, NIST SRM 610 and NIST SRM 612, *Geostand. Geoanal. Res.*, 2017, **41**, 107–122.
76 H. P. Longerich, S. E. Jackson and D. Günther, Inter-laboratory note. Laser ablation inductively coupled plasma mass spectrometric transient signal data acquisition and analyte concentration, *J. Anal. At. Spectrom.*, 1996, **11**, 899–904.
77 M. Frenzel, Making sense of mineral trace-element data – How to avoid pitfalls in statistical analysis and interpretation, *Ore Geol. Rev.*, 2023, **159**, 105566.

78 U. Kramm and K. H. Wedepohl, The isotopic composition of strontium and sulfur in seawater of Late Permian (Zechstein) age, *Chem. Geol.*, 1991, **90**, 253–262.
79 D. Rösel and T. Zack, LA-ICP-MS/MS Single-Spot Rb-Sr Dating, *Geostand. Geoanal. Res.*, 2022, **46**, 143–168.
80 A. Redaa, J. Farkaš, S. Gilbert, A. S. Collins, B. Wade, S. Löhr, T. Zack and D. Garbe-Schönberg, Assessment of elemental fractionation and matrix effects during in situ Rb-Sr dating of phlogopite by LA-ICP-MS/MS: implications for the accuracy and precision of mineral ages, *J. Anal. At. Spectrom.*, 2020, **36**, 322–344.
81 A. Redaa, J. Farkaš, S. Gilbert, A. S. Collins, S. Löhr, D. Casegh, M. Forster, M. Blades and T. Zack, Testing Nano-Powder and Fused-Glass Mineral Reference Materials for In Situ Dating of Glauconite, Phlogopite, Biotite and Feldspar via LA-ICP-MS/MS, *Geostand. Geoanal. Res.*, 2023, **47**, 23–48.
82 S. Glorie, S. E. Gilbert, M. Hand and C. Lloyd, Calibration methods for laser ablation Rb-Sr geochronology: comparisons and recommendation based on NIST glass and natural reference material, *Geochronology*, 2024, **6**, 21–36.
83 S. O. Martha, P. Xypolias, C. Cheng, W. Dörr, A. Gerdes, D. C. Hezel, M. Kutzschbach, L. Millonig, H. Schmeling, H. R. Marschall, W. Müller and G. Zulauf, Fast arc retreat in the eastern Mediterranean: constraints from late Campanian forearc deposits (Donusa, Greece), *Int. J. Earth Sci.*, 2025, **114**, 627–648.
84 P. Dezés, S. M. Schmid and P. A. Ziegler, Evolution of the European Cenozoic Rift System: interaction of the Alpine and Pyrenean orogens with their foreland lithosphere, *Tectonophysics*, 2004, **389**, 1–33.
85 J. Kley and T. Voigt, Late Cretaceous intraplate thrusting in central Europe: Effect of Africa-Iberia-Europe convergence, not Alpine collision, *Geology*, 2008, **36**, 839–842.

